Temperature driven structural evolution of Ge-rich GeSbTe alloys and role of N-doping

L. Prazakova, E. Nolot, E. Martinez, F. Fillot, D. Rouchon, N. Rochat, M. Bernard, C. Sabbione, D. Morel, N. Bernier, et al.

Temperature Driven Structural Evolution of Ge-rich GeSbTe Alloys and Role of N-doping

L. Prazakova[1], E. Nolot[1], E. Martinez[1], F. Fillot[1], D. Rouchon[1], N. Rochat[1], M. Bernard[1], C. Sabbione[1], D. Morel[1], N. Bernier[1], A. Grenier[1], A.-M. Papon[1], M.-C. Cyrille[1], G. Navarro[1]

1) Univ. Grenoble Alpes, CEA, LETI, F-38000 Grenoble, France.

Abstract

Ge-rich GeSbTe alloys allowed overcoming temperature limitations of Phase-Change Memory technology. In this paper, we present a thorough investigation of the structural evolution and crystallization process of these alloys as a function of increasing temperature of annealing. We highlight the progressive rearrangement of the structure towards the demixing of Ge and GeSbTe phases. In particular, we show the stability of Sb-Te units and the development of Ge-Te bonds around these features. We observe the formation of a transient GeSbTe phase, which is driven by crystallization phenomena, leading to a gradual diffusion and expulsion of Ge. Therefore, the system moves towards the complete separation of Ge and $Ge_2Sb_2Te_5$ stable phases. Furthermore, we investigate the effect of N doping in Ge-rich GeSbTe, which induces the formation of Ge-N bonds. Such features are demonstrated to be responsible for a delayed structural reorganization to higher temperatures, thus affecting the entire process of crystallization and phase separation in the alloy.

I. Introduction

Phase-Change Memory (PCM) is considered among the most promising Non-Volatile Memory (NVM) technologies thanks to its excellent performances such as fast programming speed, high scalability, low power consumption, good data retention and multi-level storage capability. PCM's maturity is demonstrated by its recent commercialization for Storage Class Memory (SCM) applications[1-3] and by its manufacturability and proved reliability in embedded automotive applications[4,5]. PCM has definitely passed the step of being an emerging technology, already playing an important role in the NVM market[6].

PCM device functionality is based on the reversible change between an amorphous and a crystalline phase of a chalcogenide material, accompanied by the large contrast in resistance and optical reflectivity between the two phases. Among the chalcogenide phase-change materials, $Ge_2Sb_2Te_5$ (GST225) is known as the most common reference compound for PCM whose structure and crystallization mechanism have been largely studied over the past years[7-12]. However, GST225 has a relatively low crystallization temperature of about 150 °C that is not compatible with data retention requirements of high temperature applications (i.e. automotive applications)[5,13,14]. Owing to Ge enrichment in GeSbTe alloys, PCM definitely demonstrated the capability of a high thermal stability, fulfilling the strict requirements of embedded applications[14,15]. These findings, combined with the proved benefit of N doping on retarding the crystallization to higher temperatures[16-20], raised questions about the origins of such reliability improvements. Recent investigations of Ge-rich GeSbTe (GGST) alloys highlighted the segregation of a Ge phase and a GeSbTe phase at high

temperature[21]. Moreover, transmission electron microscopy (TEM) analysis during the thermal annealing was used to suggest a two-step phase transition process, consisting of the initial crystallization of the Ge in excess, followed by the crystallization of a GeSbTe phase[22,23]. However, a complete and exhaustive structural analysis of Ge-rich GeSbTe evolution in temperature is still missing. In this work, we present the thorough investigation of the structural evolution of undoped and N-doped Ge-rich GeSbTe systems at increasing temperature. Thanks to the results coming from a wide set of complementary techniques, such as resistivity measurements, Raman spectroscopy, ex-situ and isothermal X-ray diffraction (XRD) analysis, Fourier-transform infrared spectroscopy (FTIR), transmission electron microscopy linked with energy-dispersive X-ray spectroscopy (TEM-EDX), we outline the evolution of the detected structural features until the crystallization of the layers. We highlight the importance and the stability of Sb-Te structural units along the evolution of the layer in temperature, combined with the structural rearrangement of Ge-Te bonds. Finally, we show how the same dynamic takes place in N-doped samples, but it is delayed to higher temperatures by the presence of Ge-N bonds, that play a key role on the outstanding thermal stability of Ge-rich GeSbTe alloys.

II. Experimental Methods

Amorphous 100 nm-thick layers of GST225 and GGST were deposited at room temperature on 200 mm Si (100) wafers by magnetron sputtering from pure $Ge_2Sb_2Te_5$ target (for GST225 thin layers) and by co-sputtering from Ge and $Ge_2Sb_2Te_5$ targets (for GGST thin layers) in Ar atmosphere. The nominal GGST composition considered for our study was obtained by combination of 45 % Ge and 55 % of GST225. Same Ge, Sb and Te relative content was targeted in N-doped samples. The N-doped Ge-rich GeSbTe layers (N-doped GGST) were prepared by reactive sputtering from the same targets with Ar/N_2 gas mixture in the deposition chamber. GGST layers with two different N contents were obtained by varying the ratio between Ar and N_2 gas flow during the film deposition (hereafter referred as GGSTN and $GGSTN^+$ for N_2 flow of 2 sccm and 10 sccm respectively). The layers were protected by a 3.5 nm-thick carbon capping layer to prevent surface oxidation.

To perform the measurements of sheet resistance in temperature (RvsT), 100 nm-thick layers of GST225, undoped and N-doped Ge-rich GeSbTe with similar process parameters were deposited on SiO_2 substrates and protected by a 10 nm-thick SiN capping layer. The ex-situ annealing was performed for the duration of 5 minutes, if not specified otherwise in the text, under an inert N_2 atmosphere. Four-point probe technique was used for RvsT measurements, with fixed heating rate of 10°C/min.

Raman spectra of as-deposited and annealed samples were measured at room temperature with a 532 nm laser diode excitation source (Renishaw InVia) in a range of 100 - 1000 cm^{-1}. The intensity of the laser beam was maintained at low level to avoid the changes in Raman spectra due to thermally induced structural modifications by absorption of high laser power densities. The acquisition time and number of scans were tuned to achieve a high signal to noise ratio. X-ray diffraction (XRD) data were obtained with a two-circle diffractometer (PANanalytical Empyrean) using the Cu Kα radiation (λ = 1.5406 Å). The diffraction angles were in the range from 22° to 56° (2θ) with 0.01° steps at room temperature.

III. Results

In this section, we first report on difference in crystallization temperature of undoped and N-doped GGST thin layers. After, we investigate the structural evolution of GGST thin layer, particularly by Raman spectroscopy and XRD, and finally, we analyze the effects of N-doping on the structural evolution of these alloys.

A. Resistivity-vs-Temperature Measurements

RvsT measurements performed on GeSbTe alloys are shown in **Fig. 1** and highlight the main resistivity drops of the layers in temperature. High resistivity amorphous films undergo the amorphous-to-crystalline phase transition at the crystallization temperature with a more or less sharp decrease in resistivity, related to segregation and crystallization of a low resistivity GeSbTe phase. For GST225, used as a reference for our analyses, two transitions at the temperatures of 160 °C and 330 °C can be observed for the cubic (fcc) and hexagonal (hex) phase transition, respectively[24,25].
GGST layer features a double step transition with the first drop at 300 °C and a second one slightly below 350 °C, which will be deeply investigated in the following. On the contrary, N-doped GGST layer shows a single transition at about 390 °C, confirming the higher temperature stability showed in previous works[21,26]. Higher resistivity of the crystalline state after the annealing in N-doped GGST with respect to GGST highlights the reduced progress of the segregation and the crystallization in the alloy due to N doping.

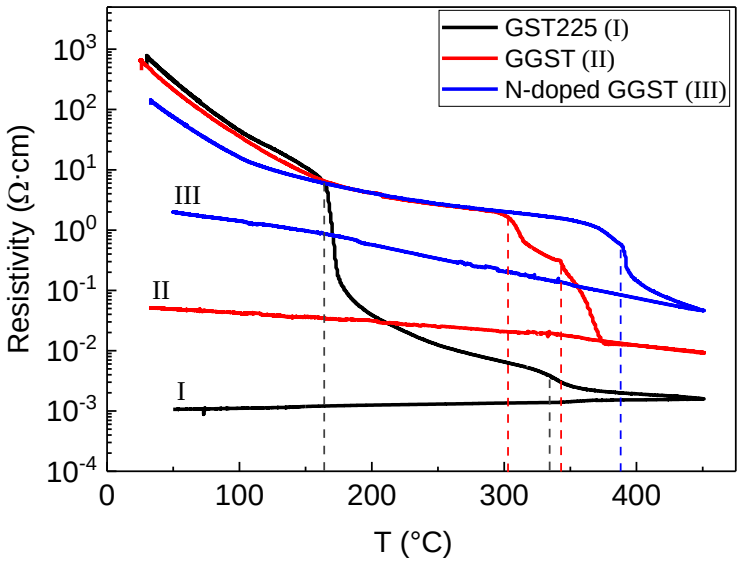

Fig. 1: RvsT measurements for GST225, GGST and N-doped GGST thin layers. Dashed lines indicate the main resistivity transitions observed in the different alloys.

B. Structural Evolution of GGST as a function of Temperature

Raman spectroscopy and XRD measurements were performed to investigate the evolution of GST225, GGST and N-doped GGST structures with increasing temperature. Raman spectra of GST225 (**Fig. 2**), which is here used as the reference material, were compared to those of Ge-rich GeSbTe layers. The Raman spectra of amorphous as-deposited (AD) GST225 is dominated by a broad feature covering the frequency region between 100 cm^{-1} and 190 cm^{-1},

formed by overlapping bands at 110 cm^{-1}, 124 cm^{-1} and 154 cm^{-1}. A low intensity band at ~ 220 cm^{-1} can also be identified. The main peak at 154 cm^{-1} can be assigned to the stretching modes of Sb-Te vibrations in $SbTe_3$ pyramidal units[27,28]. Considering the analogy with Ge-S vibration modes in GeS_2 glasses[29], the contribution of the vibration of Ge-Te tetrahedral units at about 160 cm^{-1} could also be possible, however this contribution is not visible due to much lower polarizability of Ge-Te bonds with respect to Sb-Te bonds[11]. Te-Te stretching mode, also possibly present in this frequency range[30-33], is highly unlikely in GST225[27,28]. Indeed, previous studies by extended X-ray absorption fine structure (EXAFS) show no homopolar Te-Te bonds in this alloy[34,35]. The peaks at 110 cm^{-1}, 124 cm^{-1} and 220 cm^{-1} can be assigned to the different vibrational modes of Ge-Te bonds present in tetrahedral and defective octahedral structures as observed in amorphous GeTe[9,11,36]. Below 190 cm^{-1} we mostly find vibrations of defective octahedra, whilst weaker features at high wavenumbers above 190 cm^{-1} can be assigned to Ge in tetrahedral sites[11]. In more detail, the peak at ~ 124 cm^{-1} is assigned to the A_1 vibration mode of corner-sharing tetrahedra $GeTe_{4-n}Ge_n$ (n = 1, 2) and the peaks at 110 cm^{-1} and ~ 220 cm^{-1} are assigned to the A_1 and F_2 vibration mode of $GeTe_4$ tetrahedral units, respectively[27,37].

In the spectrum of GST225 annealed at 250 °C the peak at 154 cm^{-1} ($SbTe_3$ units) remains stable, therefore characterizing even the cubic crystalline phase of the material[11,28,38]. Moreover, a new peak at 174 cm^{-1} appears, while the intensity of the peaks in the range 100 - 140 cm^{-1} (i.e. Ge-Te modes) begin to decrease. At higher annealing temperatures, the peak at 174 cm^{-1} further increases at the expense of the peak at 154 cm^{-1} ($SbTe_3$ units) which gradually disappears. This new peak was associated to the vibrations of Sb-Sb bonds in $(Te_2)Sb\text{-}Sb(Te_2)$ units where the Sb-Sb bond is connected to four Te atoms[32]. This progressive change between the peaks assigned to different Sb-Te units is evidence of the ongoing development of GST225 structure from fcc to hex crystalline phase with increasing annealing temperature.

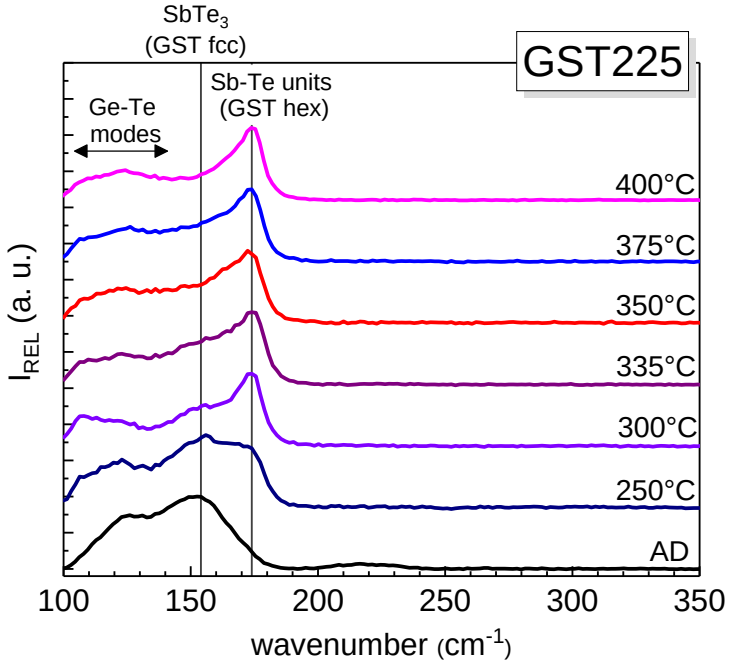

Fig. 2: Raman spectra of amorphous as-deposited (AD) and annealed GST225 (from 250 °C up to 400 °C). Vertical lines at 154 cm^{-1} and 174 cm^{-1} highlight main Sb-Te features.

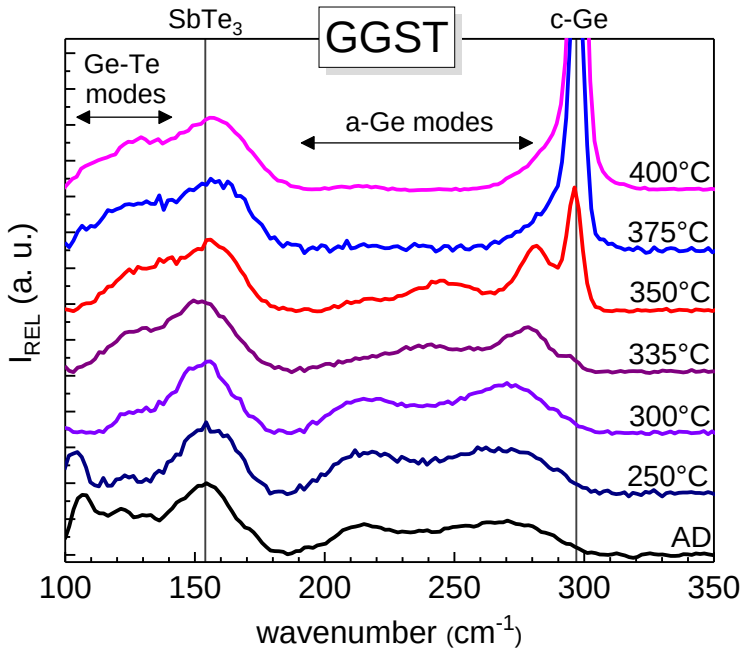

Fig. 3: Raman spectra of amorphous as-deposited (AD) and annealed GGST. Vertical lines show the position of the vibrational modes of $SbTe_3$ units (154 cm^{-1}) and crystalline Ge (297 cm^{-1}).

The Raman spectrum of as-deposited GGST (**Fig. 3**) can be divided into three main parts: I) a main peak at 154 cm^{-1} assigned to the stretching mode of $SbTe_3$ pyramidal units, already evidenced in GST225; II) features at low wavenumbers (below ~ 150 cm^{-1}) that correspond to the Ge-Te vibration modes, in agreement with previous analysis of GST225; III) features at higher wavenumbers in the range of 190 – 300 cm^{-1} which can be assigned to amorphous Ge (a-Ge) in tetrahedral sites. This broad feature is formed by two main peaks at ~ 272 cm^{-1} and ~ 230 cm^{-1} which are assigned respectively to the TO and LO vibrational modes of amorphous Ge (a-Ge)[39-42]. The peak at 154 cm^{-1} (i.e. vibration of $SbTe_3$ units), contrary to what was observed in GST225, does not significantly change either in position nor in full width at half maximum (FWHM) up to the annealing temperature of 400 °C. Ge-Te part of the spectra evidences the evolution up to 335 °C, after which it starts to be similar to the spectra of amorphous as-deposited and crystalline fcc GST225 (Fig. 2). These findings already suggest the absence of a cubic-to-hexagonal transition even at high temperature[32]. In the a-Ge part of the spectra, we observe a gradual development of TO and LO modes with increasing annealing temperature, until the new peak at 297 cm^{-1}, assigned to Ge crystalline phase (c-Ge), appears in the spectrum at 335 °C. Such temperature is particularly low for observing Ge crystallization if compared with that of an elemental a-Ge layer, normally reported to be 480 °C - 530 °C[43-46].

In order to follow the evolution trends of the above-mentioned features in GGST with temperature, we computed the sum of the peaks relative areas, obtained from the fitting of the spectra. We considered: for Ge-Te vibrational modes the peaks at 110 cm^{-1} and 124 cm^{-1}; for a-Ge modes the peaks at 220 cm^{-1} and 270 cm^{-1}; for c-Ge the peak at 297 cm^{-1}. The results were normalized with respect to the area of Sb-Te vibrational modes (main peak at 154 cm^{-1} and small contribution at 174 cm^{-1}), which remain stable in all studied temperatures. The results are shown in **Fig. 4** as a function of annealing temperature. The following evolutions can be highlighted:

T < 300°C

- Ge-Te modes, present in the amorphous as-deposited layer, initially decrease with the annealing temperature, reaching the minimum value at 300 °C. At the same time, a-Ge modes slightly increase in intensity, reaching the maximum value at 250 °C;

T > 300°C

- Ge-Te modes involved in the ordering process of the layer (i.e. crystallization of a GeSbTe phase) begin to increase after 300 °C, reaching an almost stable intensity after 375 °C;
- Simultaneously with the intensity increase of Ge-Te modes, the a-Ge modes gradually disappear, turning into the sharp peak of crystalline Ge. The c-Ge peak first appears at 335 °C and increases in intensity up to maximum annealing temperature.

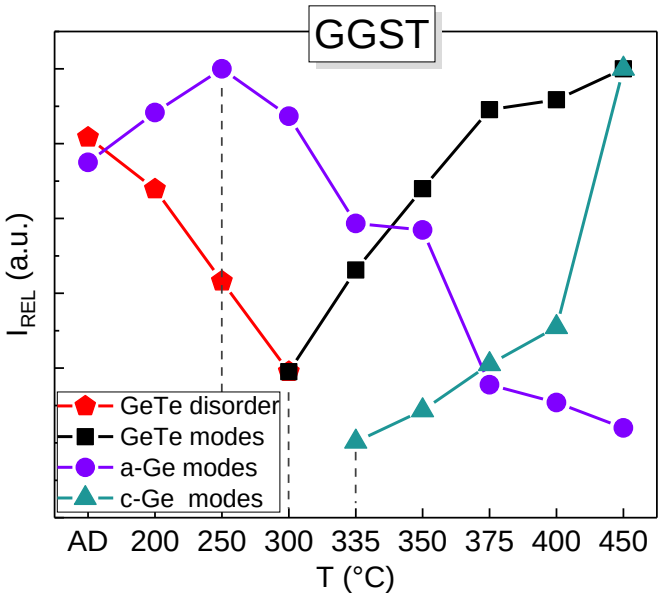

Fig. 4: Intensity evolution of Ge-Te, a-Ge and c-Ge modes from Raman spectra in GGST starting from as-deposited (AD) up to an annealing temperature of 450 °C.

We performed XRD analysis to further investigate the development of the crystalline phases in GGST (**Fig. 5**). Well-defined diffraction peaks are observed starting from the XRD pattern at 350 °C. The characteristic peaks of the fcc GST225 crystalline phase coexist with the peaks of the Ge cubic phase, which increase in intensity with the annealing temperature up to 450 °C. The XRD pattern at 335 °C features a broad band reaching the maximum at ~ 30.5° (2θ), that can be further recognized in the XRD pattern at 350 °C as a broad shoulder of the GST225 [200] main peak. Several other small peaks can be identified at 350 °C, but they disappear at higher annealing temperatures together with the above-mentioned broad band at ~ 30.5°. The presence of these features highlight a transitional step of reorganization through which the system passes before the appearance of GST225 and Ge crystalline phases. The crystallites sizes were calculated from the Scherrer's law for [220] Bragg peak of GST fcc phase and for [111] Bragg peak of Ge cubic phase (**Table 1**). GST phase shows an almost stable grain size at all the temperatures, whereas the Ge grains almost double in size from 350 °C to 450 °C.

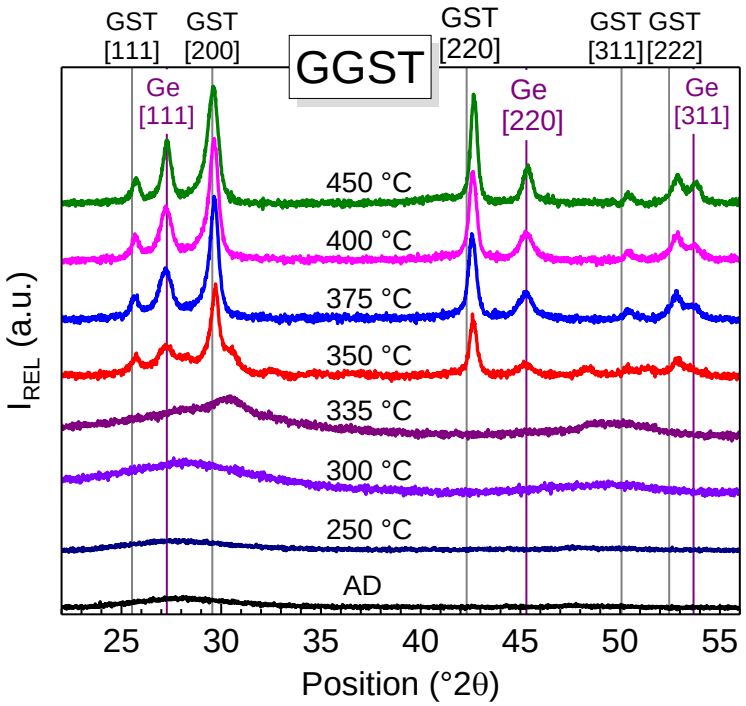

Fig. 5: XRD pattern of amorphous as-deposited (AD) and annealed GGST up to 450 °C. Indexation is performed from database data (ICDD PDF No. 00-054-0484 and 00-004-0545).

	Crystallites size [nm]	
T (°C)	**GST [220]**	**Ge [111]**
350	26	9
375	22	11
400	24	18
450	28	19

Table 1: Crystallites sizes calculated by Scherrer's law for GST and Ge phases from the XRD pattern of annealed GGST in Fig. 5.

C. N-doping Influence on Structural Evolution of GGST as a function of Temperature

Raman spectra of as-deposited and annealed GGSTN are shown in **Fig. 6**. Highly disordered structure of $GGSTN^+$ resulted in very noisy Raman spectra (thus not reported here). However, the spectra were still usable for main peaks recognition and deconvolution, which is discussed later in this section. The spectra of as-deposited and annealed N-doped layers feature the same vibrational modes recognized in GGST (Fig. 3), but the previously observed evolutions are shifted towards higher temperatures. The c-Ge peak at 297 cm^{-1}, for example, does not appear until 450 °C.

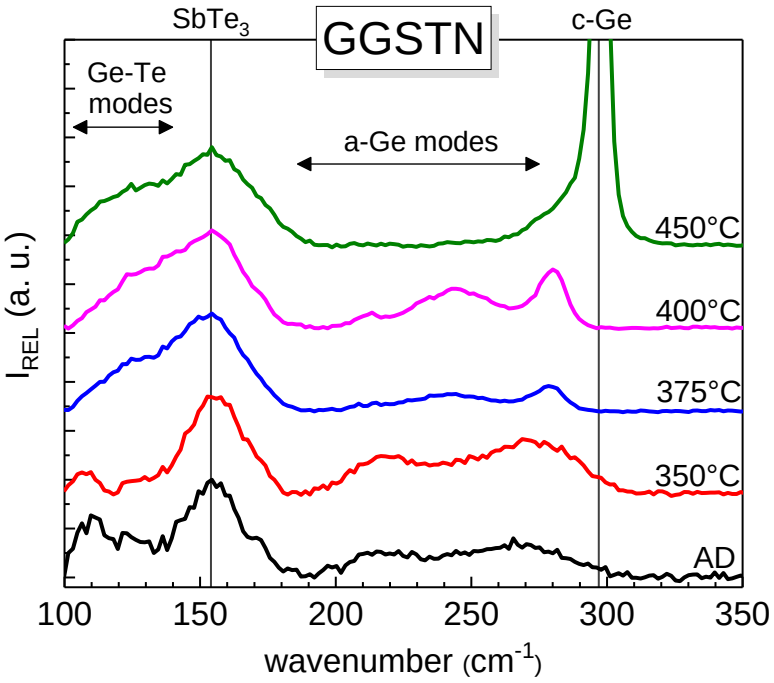

Fig. 6: Raman spectra of amorphous as-deposited (AD) and annealed GGSTN. Vertical lines show the position of the vibrational modes of $SbTe_3$ units (154 cm^{-1}) and crystalline Ge (297 cm^{-1}).

The same feature analysis as reported in Fig. 4 for GGST (integrated intensities obtained from the fitting of the spectra and normalized with respect to intensity of Sb-Te modes) was also performed on GGSTN and $GGSTN^+$. The evolution trends for Ge-Te, a-Ge modes are compared in the three layers in **Fig. 7**. For the sake of clarity, no distinction is done for Ge-Te modes before and after the detected minimum intensity, which we still attribute to the end of reordering of amorphous layer and the beginning of a GeSbTe phase crystallization. Ge-Te modes reach such minimum intensity at a temperature that increases with the N content, in particular at 300 °C, 350 °C and 400 °C for GGST, GGSTN and $GGSTN^+$ respectively. The same trend is observed for the temperature at which the maximum intensity of a-Ge modes is reached (i.e. 250 °C, 350 °C and 375 °C for GGST, GGSTN and $GGSTN^+$ respectively). Moreover, the following abrupt decrease of a-Ge modes intensity is more pronounced in the case of both N-doped GGST layers with respect to GGST. This is likely related to the crystallization of the Ge phase retarded at higher temperatures due to the N doping. Indeed, the speed of crystal growth increases with the temperature at which the nucleation takes place. In N-doped GGST samples, it leads to a faster disappearance of a-Ge modes whereas their evolution in GGST is more gradual due to its beginning at lower temperatures.

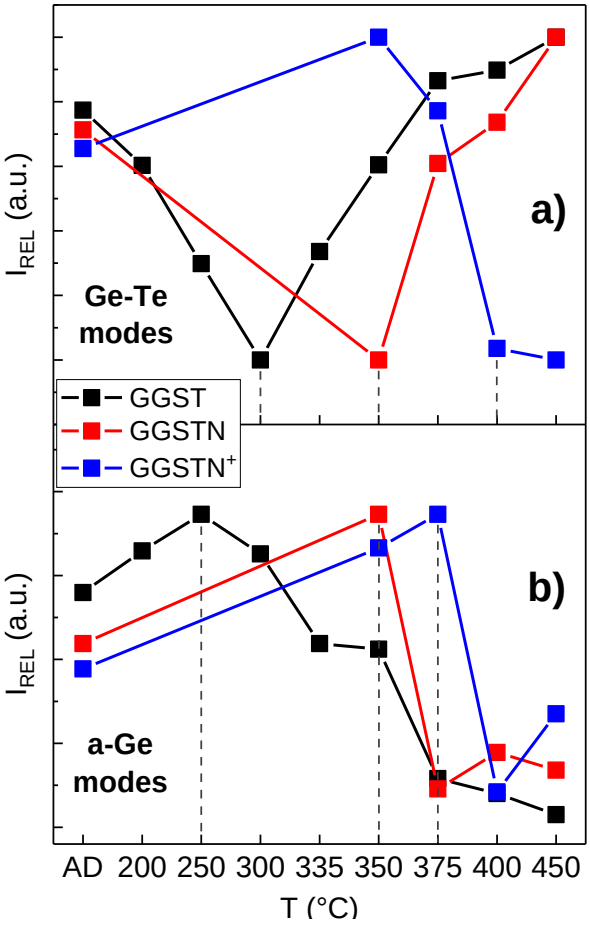

Fig. 7: Comparison of the evolution in temperature of Ge-Te (a) and a-Ge (b) modes obtained from Raman spectra in GGST, GGSTN and GGSTN$^+$. Dashed vertical lines highlight the trends inversion for both types of the modes, significant of structural transitions that are delayed to a higher temperature, the higher the nitrogen content.

XRD measurements on GGSTN samples are shown in **Fig. 8**. GGSTN$^+$ samples, however, do not show the diffraction peaks up to more than 500 °C (not reported). The first diffraction peaks in GGSTN appear at 375 °C. These diffraction peaks might correspond to the GST225 fcc phase, however their positions are significantly shifted with respect to database data (ICDD PDF No. 00-054-0484). The presence of nitrogen and the effect of annealing may induce stress and change in the lattice parameter resulting in the shift of the peak positions. However, it was previously observed that N-doping slightly increases the lattice parameter of GST fcc phase with an expected shift of the peaks at lower 2θ angles[47], which is contrary to what we observe in our spectra. The origin of such shift may be attributed to the crystallization of a transitional GeSbTe phase with Ge content higher than in GST225 (called G$^+$GST). Indeed, the 375 °C XRD pattern is compatible with several phases with stoichiometry close to $Ge_3Sb_2Te_6$ (GST326) (ICDD PDF No. 04-019-5066; 01-084-5074; 01-085-2822; 01-084-5063). N doping reduces the mobility of Ge in the alloy, which leads to the delay of the demixing process of Ge and GeSbTe phases to higher temperatures. As a result, the nucleation and growth rate of transitional G$^+$GST phase is enhanced. Therefore, the transition step is more evident in N-doped samples. In the XRD pattern at 400 °C, the GST225 fcc peaks are well identified, with the presence of the broad band at ~ 30.5°, previously highlighted in GGST at 350 °C.

The diffraction peaks of Ge crystalline phase appear only at 450 °C. The crystallites sizes were estimated as before for [220] Bragg peak of GST fcc phase and for [111] Bragg peak of Ge crystalline phase (**Table 2**), confirming the delayed nucleation and growth of the identified phases.

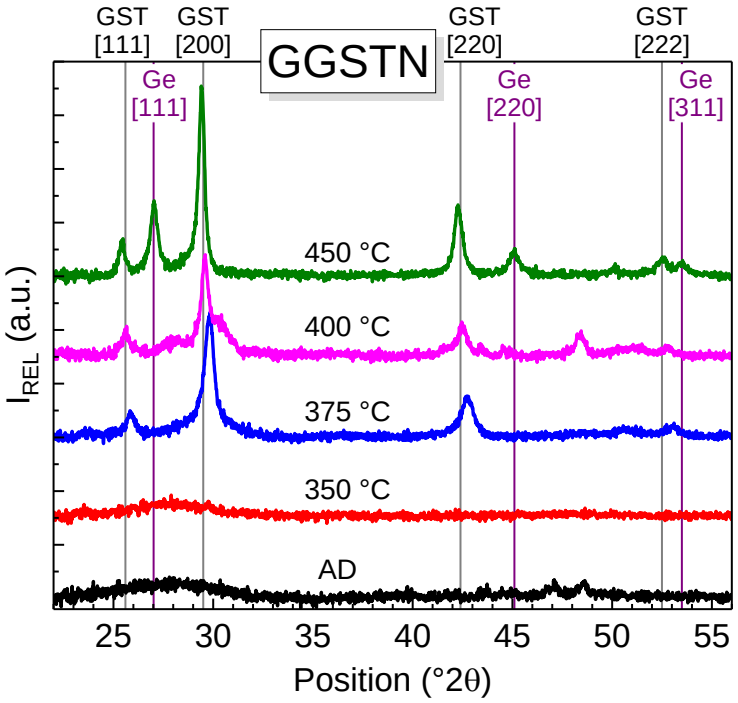

Fig. 8: XRD pattern of amorphous as-deposited (AD) and annealed GGSTN up to 450 °C. Indexation is performed from database data (ICDD PDF No. 00-054-0484 and 00-004-0545).

	Crystallite size [nm]	
T (°C)	**GST [220]**	**Ge [111]**
350	/	/
375	/	/
400	16	/
450	21	19

Table 2: Crystallites sizes calculated by Scherrer's law for GST and Ge phases from the XRD pattern of annealed GGSTN in Fig. 8.

N-doped GGST layers were further investigated by FTIR spectroscopy to support the previous results of Raman and XRD analysis. It is known that in N-doped GGST alloys, nitrogen tends to principally bond with Ge, forming thus the Ge-N bonds[48–53]. A considerable charge transfer from Ge to N produces strong IR absorption bands related to the Ge-N bond structure well detectable by FTIR spectroscopy. IR spectra of both GGSTN and GGSTN$^+$ are shown in **Fig. 9**. In order to understand the impact of the presence of Sb and Te in GGST layers, we also prepared and analyzed N-doped single-element Ge thin layers (hereafter referred as GeN and GeN$^+$) with the same thickness and with the N incorporation close to N-doped GGST compositions. In both Ge and GGST layers, the main absorption band

centered at ~ 700 cm^{-1} is assigned to the in-plane asymmetric stretching vibration of Ge_3N skeletal group[39]. In GeN^+ and $GGSTN^+$ spectra, a second contribution at higher wavenumbers (750 - 830 cm^{-1}) appears, forming the large shoulder to the main absorption band. This second contribution is also ascribed to Ge-N stretching vibrations, but shifted to the higher wavenumber (with respect to the main peak at ~ 700 cm^{-1}). The shift is the result of the inductive effect of higher nitrogen content, which is creating different chemical environment around the Ge atoms[39].

The increasing temperature does not affect N-doped Ge layers, where the main broad band of Ge-N vibration remains stable in position and FWHM. On the contrary, a significant shift of up to ~ 40 cm^{-1} (at 450 °C) to the higher wavenumbers is observed in GGSTN spectra as the annealing temperature increases. A similar shift is also observed in the spectra of $GGSTN^+$, but reduced in size to ~ 10 cm^{-1}. As reported before, the shift to higher wavenumbers is due to a gradual change of the Ge and N atoms arrangement, in particular correlated to the impoverishment in Ge around the main Ge-N vibration. The trend is particularly evident in GGSTN where the crystallization of the layer is more advanced with respect to $GGSTN^+$ in the range of temperatures of our analysis. The comparison of almost unchanged spectra of GeN and GeN^+ with spectra of GGSTN and $GGSTN^+$, reveals the effect of the ongoing crystallization of a GeSbTe phase on the nucleation of Ge and consequently on the perturbation of Ge-N system.

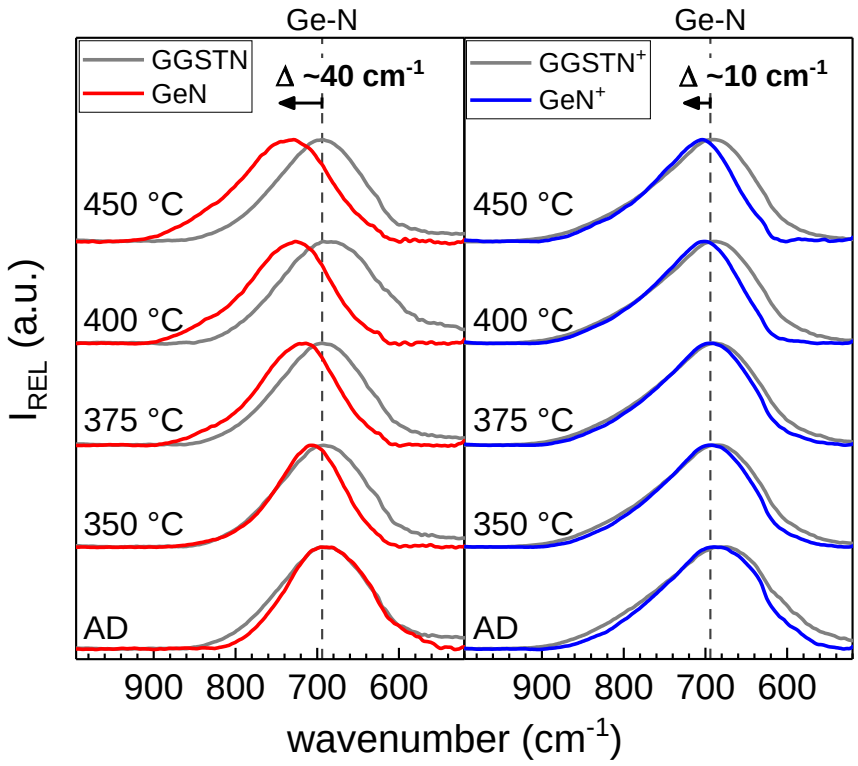

Fig. 9: FTIR spectra of amorphous as-deposited (AD) and annealed N-doped Ge and GGST.

IV. Discussions and Complementary Experiments

Combining all the previous results from Raman, XRD and FTIR analysis in section III, we can finally highlight the main structural evolutions of Ge-rich GeSbTe alloys as a function of the annealing temperature.

The as-deposited GGST sample features amorphous structure (XRD analysis, Fig. 5), which is usually associated with high level of disorder. Raman spectroscopy, however, reveals the vibration modes of structural Sb-Te units, which can be considered as the basis of the structure of GeSbTe alloys. It is important to note that these Sb-Te structural units remain stable from amorphous as-deposited samples up to samples annealed at high temperatures (Fig. 3).

The initial increase of the temperature up to 300 °C results in a first reorganization step, characterized by the decrease of Ge-Te modes and simultaneous enhancement of a-Ge modes (Fig. 4). Indeed, the breakage of unfavorable bonding in mixed GeSbTe units (e. g. $GeSbTe_3$, Ge_2SbTe_2 or $GeSb_2Te_2$ [54,55]) and the rearrangement of $GeTe_{4-n}Ge_n$ (n=0, 1, 2, 3, 4) tetrahedral units may occur in originally amorphous disordered system, both resulting in reduction of the Ge-Te modes. As a consequence, the overcoordinated Ge atoms in the mixed units are liberated, increasing the intensity of a-Ge modes. This is in agreement with previous investigations on amorphous GeTe alloys[37], based on the random bonding model[56], in which the combination of the different tetrahedra complex units depends also on the layer stoichiometry. The observed reorganization at low temperatures is also present in N-doped layers (Fig. 7); however, the reorganization process is prolonged up to a higher temperature due to the delay induced by N doping.

The structural evolution is more significant at annealing temperatures above 300 °C. At this temperature, the Ge-Te modes evidence the minimum value (Fig. 7) related to the end of the first reorganization step. Higher annealing temperatures evidence the progressive increase of Ge-Te modes, which indicates the gradual rearrangement of Ge-Te bonds around Sb-Te features inside the crystalline GeSbTe phase. The crystalline GeSbTe phase then further nucleates and grows in the layer. On the contrary, disappearing of a-Ge modes at temperatures above 300 °C is associated with the reorganization of Ge structure and with the consequent nucleation and growth of Ge cubic phase (Fig. 3 and Fig. 5). N doping leads to the formation of Ge-N bond, affecting the mobility of Ge atoms. As a result, the demixing of GeSbTe and Ge phases as well as the process of nucleation of a GeSbTe phase are delayed to higher temperature.

XRD analyses on both GGST and GGSTN samples showed the appearance of an intermediate structural evolution step at ~ 30.5° (2θ) (at 350 °C for GGST in Fig. 5, and at 400 °C for GGSTN in Fig. 8). Combining the results from GGST and GGSTN, we can suggest the formation of a transient phase (G^+GST), which features higher Ge content with respect to standard GST225. Evidence of such double step crystallization can be already found in RvsT measurement of GGST in Fig. 1. In addition, the G^+GST transient phase can even grow, as observed in GGSTN (Fig. 8) if the temperature and the duration of the annealing are high enough. To confirm the hypothesis of transient G^+GST phase, we performed isothermal XRD measurements for the duration of 70 hours (**Fig. 10**). The temperature of the isothermal annealing was kept at ~ 300 °C, i.e. the temperature at which the first changes in XRD spectra are observed in Fig. 5 for GGST. The aim was to sufficiently slow down the entire mechanism and therefore to achieve the clear sequence of the different phases appearing in the spectra. The G^+GST broad band appears in the spectra after about one hour of annealing. After only few hours, the [200] main peak of GST225 cubic phase starts to increase. The intensity of G^+GST peak then decreases progressively as the intensity of the GST [200] peak increases. The gradual expulsion of Ge from G^+GST continues in favor of the crystallization

of more stable GST225 phase. This is rather in agreement with previous observations on a crystallization-induced segregation in Te-rich GeSbTe materials[57]. More than 30 hours of annealing are required to initiate the growth of Ge crystals, when Ge is finally accumulated on the grain boundaries outside of GeSbTe crystalline regions. The presence of GeSbTe crystalline interfaces likely induces the heterogeneous nucleation of Ge, followed by the rapid growth of Ge crystallites. The rapid growth of Ge crystalline phase overtakes the crystallization dynamics of the system and limits the further development of GeSbTe crystals (i.e. crystallite size of GST225 remains constant with temperature, as shown in Table 1). Heterogeneous nucleation of Ge from the neighbor seed crystal allows Ge to crystallize at the temperatures lower than at elemental a-Ge layers, as observed in Fig. 3.

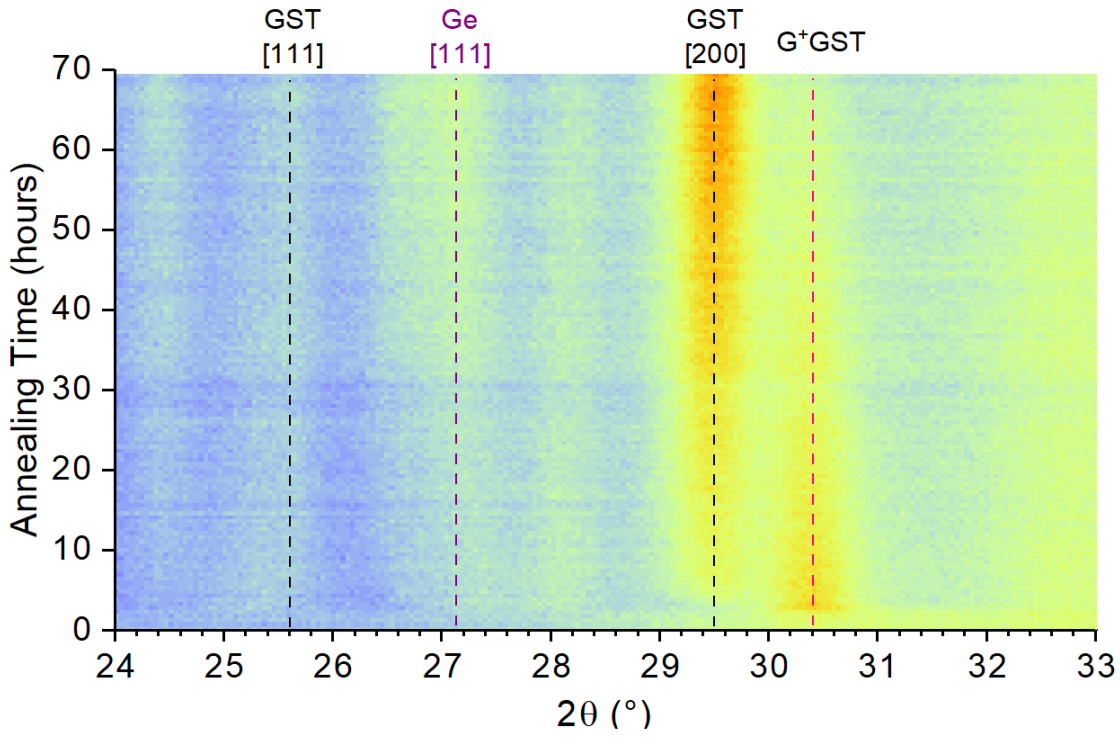

Fig. 10: Isothermal XRD measurements at ~ 300 °C on GGST showing the development of GST225 and Ge crystalline phase (black and violet dashed lines, respectively). A transient G⁺GST phase (red dashed line) is detected before the appearance of GST225 phase.

The main compositional steps of the GeSbTe phase developed in GGST layer in temperature are evidenced in **Fig. 11**. The Ge over Te ratio in GGST samples approaches 2:1. GST225, however, lies on the line between Sb_2Te_3 and GeTe where Ge over Te ratio is close to 1:1. As the Ge mobility increases in temperature, the local organization of the structure around the stable Sb-Te features drives the system locally towards a gradual expulsion of Ge, giving rise to a G⁺GST transient phase. The nucleation and growth of this G⁺GST transient phase then continues to feed the demixing process. The red circle in Fig. 11 highlights the region around GST326 in which possible transient phases can be found. Following this evolution, Ge-Te features evolve until a stable configuration of GST225 is reached (saturation observed in Fig. 4).

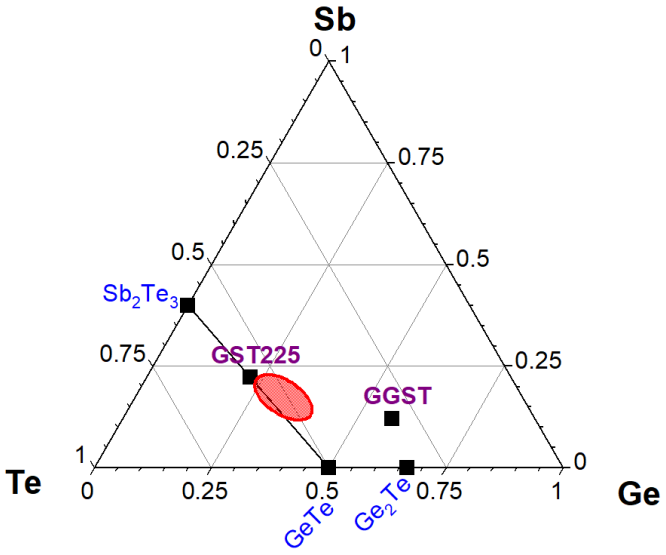

Fig. 11: Ge-Sb-Te ternary diagram highlighting GST225 and GGST compositions. Red circle indicates the region (around GST326) of the transient G⁺GST phase that can give rise to start of partial crystallization in GGST as observed in XRD analyses.

We performed the TEM-EDX images on GGST samples (**Fig. 12**), in order to follow the demixing process in the alloy. The image of as-deposited (AD) layer indicates the perfect homogeneity of the prepared amorphous alloy. An elemental migration is already visible at 300 °C, which correspond to the end point of the first reorganization step, as observed by Raman spectroscopy (Fig. 3 and Fig. 4). The migration becomes more evident at 380 °C where the Ge-rich and Sb/Te-rich regions are already clearly separated. Formation of such regions evidences the demixing process of Ge and GeSbTe phase described above. Separated Ge-rich regions confirm the XRD findings (Fig. 5), where the already developed Ge crystalline phase is observed around this temperature. The phase separation is fully completed at 450 °C where the perfectly formed Ge and GeSbTe crystalline phases can be distinguished. Yellow squares in Fig. 12 highlight a region with GeSbTe grain. The crystallization growth of separated Ge and GeSbTe phases dominates the system at this temperature (crystallite sizes in Table 1).

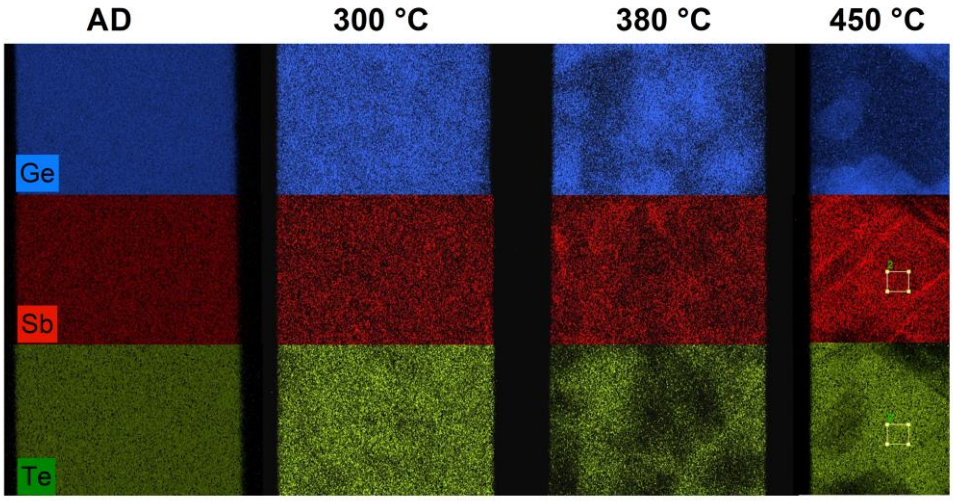

Fig. 12: TEM-EDX analyses of GGST samples: amorphous as-deposited (AD) and annealed at 300 °C, 380 °C and 450 °C. Ge, Sb and Te cartographies highlight the ongoing demixing process.

As mentioned above, N doping retards the Ge diffusivity due to the formation of Ge-N bonds (Fig. 9) and delays the appearance of a GeSbTe crystalline phase to higher temperature. Besides, the nucleation rate and the growth speed increase with the temperature. Therefore, the G^+GST phase can develop clear peaks in XRD spectra before the final transition towards a more stable GST225 phase (at 375 °C in Fig. 8). Continuous expulsion of Ge during the formation of the GST225 phase leads to the coexistence of crystalline GST225 and G^+GST surrounded by Ge in excess. Ge crystalline phase appears only after the full development of the GST225 phase, which is clearly observed in GGSTN samples (development of c-Ge peak at 450 °C in Fig. 8). Indeed, the important role of N-doping in the delay of Ge crystallization is confirmed by FTIR results (Fig. 9), which highlight the gradual reduction of Ge atoms involved in Ge-N features. Ge-N bonds (E_{Ge-N} ~ 2.65 eV) are stronger than Ge-Ge (E_{Ge-Ge} ~ 1.94 eV)[39] and require higher annealing temperature for breaking. As discussed in section III, the shift of the peak energy of dipole vibration at higher wavenumbers, is associated with the change of Ge and N environment (Ge-N in different bonding configurations), in particular with an impoverishment in Ge[39] around the Ge-N bonds. The liberated Ge is then progressively involved in the crystallization process of a Ge cubic phase. Moreover, the presence of Te atoms in the environment of Ge-N bonds may also affect the IR shift presented in Fig. 9 and should be a subject of another study.
The overall review of the steps of the structural evolution of GGST and GGSTN as a function of annealing temperatures is shown in **Fig. 13**.

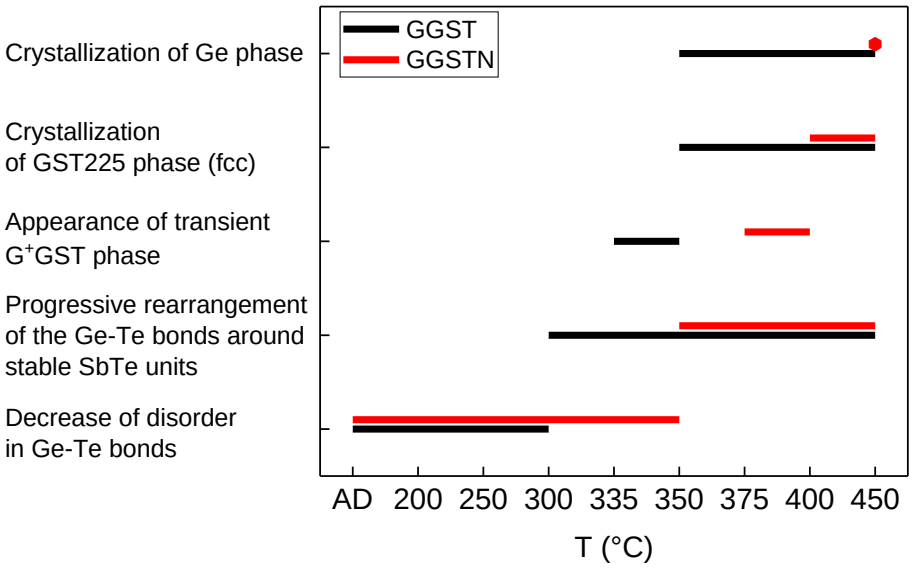

Fig. 13: Diagram summarizing the main features highlighted in this work related to the structural evolution of GGST (black, bottom bars) and GGSTN (red, top bars) with annealing temperature.

V. Conclusions

In this work, we presented a thorough investigation of the structural evolution of undoped and N-doped Ge-rich GeSbTe phase-change materials with annealing temperature. Thanks to a wide set of techniques, such as Raman and FTIR spectroscopy, XRD, TEM-EDX, we

observed the stability of the Sb-Te structural units in these alloys at increasing temperature and the gradual structural rearrangement of Ge-Te bonds around these units. We deeply investigated the mechanism of crystallization of GGST starting with the crystallization of a GeSbTe transient phase with higher Ge content than GST225 phase (G^+GST) and consequent progressive expulsion of Ge. The system moves towards a complete separation of Ge and GST225 phases. After the GeSbTe stable phase is reached, the GeSbTe grains serves as a seeds for heterogeneous nucleation and crystallization of the Ge phase. Nitrogen in the as-deposited N-doped GGST layer leads to the formation of Ge-N bonds and reduces the Ge mobility. As a result, the process rearrangement of Ge-Te bonds and the global crystallization dynamic of the layer are delayed. Indeed, Ge-N bonds present in the layer affect the entire demixing process of Ge and GST225 phases, leading to the outstanding stability of N-doped Ge-rich GeSbTe materials at high temperatures.

Acknowledgments

This work has been performed with the help of the NanoCaracterization Platform of Minatec with the financial support of the "Recherche Technologique de Base" program. It has been partially supported by the European 783176 WAKeMeUP Project, financed by European commission, French government and Auvergne-Rhône Alpes Region.

Data Availability

The data that support the findings of this study are available from the corresponding author upon reasonable request.

References

[1] H.-Y. Cheng, F. Carta, W.-C. Chien, H.-L. Lung, and M.J. BrightSky, J. Phys. Appl. Phys. **52**, 473002 (2019).

[2] https://www.micron.com/products/advanced-solutions/3d-xpoint-technology, Micron (n.d.).

[3] https://www.intel.co.uk/content/www/uk/en/architecture-and-technology/optane-memory.html, Intel (n.d.).

[4] F. Arnaud, P. Zuliani, J.P. Reynard, A. Gandolfo, F. Disegni, P. Mattavelli, E. Gomiero, G. Samanni, C. Jahan, R. Berthelon, O. Weber, E. Richard, V. Barral, A. Villaret, S. Kohler, J.C. Grenier, R. Ranica, C. Gallon, A. Souhaite, D. Ristoiu, L. Favennec, V. Caubet, S. Delmedico, N. Cherault, R. Beneyton, S. Chouteau, P.O. Sassoulas, A. Vernhet, Y. Le Friec, F. Domengie, L. Scotti, D. Pacelli, J.L. Ogier, F. Boucard, S. Lagrasta, D. Benoit, L. Clement, P. Boivin, P. Ferreira, R. Annunziata, and P. Cappelletti, in *2018 IEEE Int. Electron Devices Meet. IEDM* (IEEE, San Francisco, CA, 2018), p. 18.4.1-18.4.4.

[5] P. Cappelletti, R. Annunziata, F. Arnaud, F. Disegni, A. Maurelli, and P. Zuliani, J. Phys. Appl. Phys. **53**, 193002 (2020).

[6] G. Navarro, G. Bourgeois, J. Kluge, A.L. Serra, A. Verdy, J. Garrione, M.-C. Cyrille, N. Bernier, A. Jannaud, C. Sabbione, M. Bernard, E. Nolot, F. Fillot, P. Noe, L. Fellouh, G. Rodriguez, V. Beugin, O. Cueto, N. Castellani, J. Coignus, V. Delaye, C. Socquet-Clerc, T. Magis, C. Boixaderas, S. Barnola, and E. Nowak, in *2018 IEEE Int. Mem. Workshop IMW* (IEEE, Kyoto, 2018), pp. 1–4.

[7] A.V. Kolobov, P. Fons, A.I. Frenkel, A.L. Ankudinov, J. Tominaga, and T. Uruga, Nat. Mater. **3**, 703 (2004).

[8] A.V. Kolobov, P. Fons, and J. Tominaga, Phys. Status Solidi B **246**, 1826 (2009).

[9] S. Caravati, M. Bernasconi, T.D. Kühne, M. Krack, and M. Parrinello, Appl. Phys. Lett. **91**, 171906 (2007).
[10] S. Caravati, M. Bernasconi, T.D. Kühne, M. Krack, and M. Parrinello, J. Phys. Condens. Matter **21**, 255501 (2009).
[11] G.C. Sosso, S. Caravati, R. Mazzarello, and M. Bernasconi, Phys. Rev. B **83**, 134201 (2011).
[12] K. Shportko, L. Revutska, O. Paiuk, J. Baran, A. Stronski, A. Gubanova, and E. Venger, Opt. Mater. **73**, 489 (2017).
[13] S. Raoux, H.-Y. Cheng, J. Sandrini, J. Li, and J. Jordan-Sweet, in *2011 11th Annu. Non-Volatile Mem. Technol. Symp. Proceeding* (IEEE, Shanghai, China, 2011), pp. 1–5.
[14] P. Zuliani, E. Varesi, E. Palumbo, M. Borghi, I. Tortorelli, D. Erbetta, G.D. Libera, N. Pessina, A. Gandolfo, C. Prelini, L. Ravazzi, and R. Annunziata, IEEE Trans. Electron Devices **60**, 4020 (2013).
[15] P. Zuliani, F. Disegni, L. Croce, and R. Annunziata, in *2019 IEEE 11th Int. Mem. Workshop IMW* (IEEE, Monterey, CA, USA, 2019), pp. 1–4.
[16] S. Privitera, E. Rimini, C. Bongiorno, A. Pirovano, and R. Bez, Nucl. Instrum. Methods Phys. Res. Sect. B Beam Interact. Mater. At. **257**, 352 (2007).
[17] I. Yang, K. Do, H.-J. Chang, D.-H. Ko, and H. Sohn, J. Electrochem. Soc. **157**, H483 (2010).
[18] L.W.-W. Fang, R. Zhao, M. Li, K.-G. Lim, L. Shi, T.-C. Chong, and Y.-C. Yeo, J. Appl. Phys. **107**, 104506 (2010).
[19] D. Yao, X. Zhou, L. Wu, Z. Song, L. Cheng, F. Rao, B. Liu, and S. Feng, Solid-State Electron. **79**, 138 (2013).
[20] H.Y. Cheng, J.Y. Wu, R. Cheek, S. Raoux, M. BrightSky, D. Garbin, S. Kim, T.H. Hsu, Y. Zhu, E.K. Lai, E. Joseph, A. Schrott, S.C. Lai, A. Ray, H.L. Lung, and C. Lam, in *2012 Int. Electron Devices Meet.* (IEEE, San Francisco, CA, USA, 2012), p. 31.1.1-31.1.4.
[21] V. Sousa, G. Navarro, N. Castellani, M. Coue, O. Cueto, C. Sabbione, P. Noe, L. Perniola, S. Blonkowski, P. Zuliani, and R. Annunziata, in *2015 Symp. VLSI Technol. VLSI Technol.* (IEEE, Kyoto, Japan, 2015), pp. T98–T99.
[22] M. Agati, F. Renaud, D. Benoit, and A. Claverie, MRS Commun. **8**, 1145 (2018).
[23] M. Agati, M. Vallet, S. Joulié, D. Benoit, and A. Claverie, J. Mater. Chem. C **7**, 8720 (2019).
[24] N. Yamada, E. Ohno, K. Nishiuchi, N. Akahira, and M. Takao, J. Appl. Phys. **69**, 2849 (1991).
[25] I. Friedrich, V. Weidenhof, W. Njoroge, P. Franz, and M. Wuttig, J. Appl. Phys. **87**, 4130 (2000).
[26] P. Zuliani, E. Palumbo, M. Borghi, G. Dalla Libera, and R. Annunziata, Solid-State Electron. **111**, 27 (2015).
[27] K.S. Andrikopoulos, S.N. Yannopoulos, A.V. Kolobov, P. Fons, and J. Tominaga, J. Phys. Chem. Solids **68**, 1074 (2007).
[28] P. Němec, A. Moreac, V. Nazabal, M. Pavlišta, J. Přikryl, and M. Frumar, J. Appl. Phys. **106**, 103509 (2009).
[29] R. De Bastiani, A.M. Piro, M.G. Grimaldi, E. Rimini, G.A. Baratta, and G. Strazzulla, Appl. Phys. Lett. **92**, 241925 (2008).
[30] B.H. Torrie, Solid State Commun. **8**, 1899 (1970).
[31] J. Tominaga and N. Atoda, Jpn. J. Appl. Phys. **38**, L322 (1999).
[32] B. Liu, S. Zhi-Tang, Z. Ting, F. Song-Lin, and C. Bomy, Chin. Phys. **13**, 1947 (2004).
[33] H. Satoh, K. Sugawara, and K. Tanaka, J. Appl. Phys. **99**, 024306 (2006).
[34] D.A. Baker, M.A. Paesler, G. Lucovsky, S.C. Agarwal, and P.C. Taylor, Phys. Rev. Lett. **96**, 255501 (2006).

[35] M.A. Paesler, D.A. Baker, and G. Lucovsky, J. Non-Cryst. Solids **354**, 2706 (2008).
[36] R. Mazzarello, S. Caravati, S. Angioletti-Uberti, M. Bernasconi, and M. Parrinello, Phys. Rev. Lett. **104**, 085503 (2010).
[37] K.S. Andrikopoulos, S.N. Yannopoulos, G.A. Voyiatzis, A.V. Kolobov, M. Ribes, and J. Tominaga, J. Phys. Condens. Matter **18**, 965 (2006).
[38] Z. Xu, C. Chen, Z. Wang, K. Wu, H. Chong, and H. Ye, RSC Adv. **8**, 21040 (2018).
[39] I. Chambouleyron and A.R. Zanatta, J. Appl. Phys. **84**, 1 (1998).
[40] P. Kazimierski, J. Tyczkowski, M. Kozanecki, Y. Hatanaka, and T. Aoki, Chem. Mater. **14**, 4694 (2002).
[41] H. Jamali, R. Mozafarinia, and A. Eshaghi, J. Alloys Compd. **646**, 360 (2015).
[42] H. Jamali, R. Mozafarinia, and A. Eshaghi, Surf. Coat. Technol. **310**, 1 (2017).
[43] F. Katsuki, K. Hanafusa, M. Yonemura, T. Koyama, and M. Doi, J. Appl. Phys. **89**, 4643 (2001).
[44] A.F. Khan, M. Mehmood, A.M. Rana, and T. Muhammad, Appl. Surf. Sci. **256**, 2031 (2010).
[45] Q. Tao, N. Chen, C. Wang, M. Dayan, Y. Bai, and J. Chen, Mater. Sci. Semicond. Process. **84**, 167 (2018).
[46] C.-Y. Tsao, J.W. Weber, P. Campbell, P.I. Widenborg, D. Song, and M.A. Green, Appl. Surf. Sci. **255**, 7028 (2009).
[47] F. Fillot, C. Sabbione, F. Pierre, F. Hippert, and P. Noé, J. Appl. Crystallogr. **51**, 1691 (2018).
[48] B. Liu, Z. Song, T. Zhang, J. Xia, S. Feng, and B. Chen, Thin Solid Films **478**, 49 (2005).
[49] Y. Kim, K. Jeong, M.-H. Cho, U. Hwang, H.S. Jeong, and K. Kim, Appl. Phys. Lett. **90**, 171920 (2007).
[50] K.B. Borisenko, Y. Chen, S.A. Song, and D.J.H. Cockayne, Chem. Mater. **21**, 5244 (2009).
[51] K.-H. Kim, J.-C. Park, J.-H. Lee, J.-G. Chung, S. Heo, and S.-J. Choi, Jpn. J. Appl. Phys. **49**, 101201 (2010).
[52] G. Navarro, V. Sousa, P. Noe, N. Castellani, M. Coue, J. Kluge, A. Kiouseloglou, C. Sabbione, A. Persico, A. Roule, O. Cueto, S. Blonkowski, F. Fillot, N. Bernier, R. Annunziata, M. Borghi, E. Palumbo, P. Zuliani, and L. Perniola, in *2016 IEEE 8th Int. Mem. Workshop IMW* (IEEE, Paris, France, 2016), pp. 1–4.
[53] E. Nolot, C. Sabbione, W. Pessoa, L. Prazakova, and G. Navarro, Appl. Surf. Sci. (2020).
[54] P. Jóvári, I. Kaban, J. Steiner, B. Beuneu, A. Schöps, and A. Webb, J. Phys. Condens. Matter **19**, 335212 (2007).
[55] P. Jóvári, I. Kaban, J. Steiner, B. Beuneu, A. Schöps, and M.A. Webb, Phys. Rev. B **77**, 035202 (2008).
[56] H.R. Philipp, J. Non-Cryst. Solids **8**–**10**, 627 (1972).
[57] A. Debunne, K. Virwani, A. Padilla, G.W. Burr, A.J. Kellock, V.R. Deline, R.M. Shelby, and B. Jackson, J. Electrochem. Soc. **158**, H965 (2011).